Graphene nanoribbons with hBN passivated edges grown by high-temperature molecular beam epitaxy

2D Materials

OPEN ACCESS

RECEIVED
3 February 2023

REVISED
9 June 2023

ACCEPTED FOR PUBLICATION
16 June 2023

PUBLISHED
29 June 2023

PAPER

Graphene nanoribbons with hBN passivated edges grown by high-temperature molecular beam epitaxy

Jonathan Bradford[1,*], **Tin S Cheng**[1], **Tyler S S James**[1], **Andrei N Khlobystov**[2], **Christopher J Mellor**[1], **Kenji Watanabe**[3], **Takashi Taniguchi**[3], **Sergei V Novikov**[1] and **Peter H Beton**[1,*]

[1] School of Physics and Astronomy, University of Nottingham, Nottingham NG7 2RD, United Kingdom
[2] School of Chemistry, University of Nottingham, Nottingham NG7 2RD, United Kingdom
[3] National Institute for Materials Science, 1-1 Namiki, Tsukuba 305-0044, Japan
[*] Authors to whom any correspondence should be addressed.

E-mail: jonathan.bradford@nottingham.ac.uk and peter.beton@nottingham.ac.uk

Keywords: graphene nanoribbons, hexagonal boron nitride, lateral heterostructure, conductive AFM, molecular beam epitaxy, nanoparticle etching

Supplementary material for this article is available online

Abstract

Integration of graphene and hexagonal boron nitride (hBN) in lateral heterostructures has provided a route to broadly engineer the material properties by quantum confinement of electrons or introduction of novel electronic and magnetic states at the interface. In this work we demonstrate lateral heteroepitaxial growth of graphene nanoribbons (GNRs) passivated by hBN using high-temperature molecular beam epitaxy (HT-MBE) to grow graphene in oriented hBN trenches formed *ex-situ* by catalytic nanoparticle etching. High-resolution atomic force microscopy (AFM) reveals that GNRs grow epitaxially from the etched hBN edges, and merge to form a GNR network passivated by hBN. Using conductive AFM we probe the nanoscale electrical properties of the nanoribbons and observe quasiparticle interference patterns caused by intervalley scattering at the graphene/hBN interface, which carries implications for the potential transport characteristics of hBN passivated GNR devices.

1. Introduction

Graphene and hexagonal boron nitride (hBN) have become the cornerstones of two-dimensional (2D) electronics as an exceptional conductor and dielectric, respectively. Due to the small lattice mismatch (∼1.8%) of graphene and hBN it is possible to form lateral heterojunctions between the two materials leading to new opportunities for the fabrication of atomically thin devices and circuitry [1–3]. Lateral heterostructures of graphene and hBN have attracted interest due to their widely tuneable electronic properties, and potential to exploit the spin properties of the interface [4–6]. Broadly, the properties of lateral graphene/hBN heterostructures can be tuned according to the relative concentrations of carbon and hBN, size and geometry of the domains, and the structure of the interface [7–12]. One interesting system to consider is the formation of hBN-passivated graphene nanoribbons (GNRs). In these structures, the electronic properties of the GNRs are dictated by the width of the nanoribbons, and the structure of the interface formed with hBN. For GNRs with an armchair-oriented interface, a bandgap can be opened by quantum confinement as the width of the GNR is reduced, while the interface remains electronically passive due to the alternating B–C and C–N bonding along both sides of the nanoribbon [10, 11, 13]. Alternatively, zig-zag GNRs form polar interfaces with hBN with spin-polarised edge states, and are predicted to exhibit half-metallicity [5, 6, 10, 11, 14]. To realise and exploit these effects, controlled orientation and interface formation in hBN passivated GNRs is imperative.

The formation of 2D lateral heterostructures of graphene and hBN has been reported using multiple techniques such as chemical vapour deposition (CVD) [1, 2, 15–20], high-temperature molecular beam epitaxy (HT-MBE) [21, 22], and substitutional doping or chemical conversion [23–25]. For CVD and MBE-based approaches, GNRs can be formed

by edge-templated growth of graphene from hBN edges. Recently, chirality controlled hBN edges have been formed in exfoliated hBN flakes by local catalytic hydrogen etching using transition metal nanoparticles (NPs) [26–29]. This has enabled templated growth of GNRs embedded in hBN by subsequent graphene growth using plasma-enhanced CVD [26, 28]. Transport measurements in these works demonstrated respectable carrier mobilities of $\sim$1500 cm^2 V^{-1} s^{-1} and scattering mean-free paths of 50–80 nm, suggesting high quality interfaces, but details of carrier scattering at the interface remains unknown.

In this work we demonstrate lateral heteroepitaxial growth of GNRs on nickel (Ni) NP etched hBN flakes by HT-MBE. Catalytic directional etching of the hBN flakes by Ni NPs produces a predominantly zigzag oriented network of monolayer deep hBN trenches which form a template for GNR growth. We study the early growth stages of the GNRs using high-resolution atomic force microscopy (AFM) and show that the growth rate differs between B-terminated and N-terminated zigzag edges at elevated temperatures. Using conductive AFM (cAFM) we show that fully grown GNRs form a conductive network embedded in the hBN surface, and show evidence of intervalley scattering at the graphene/hBN interface which, we argue, is likely to influence the transport properties of the GNRs.

2. Experimental details

2.1. Substrate preparation

Substrates were prepared by mechanical exfoliation of hBN single bulk crystals onto single-side polished sapphire, graphitised silicon carbide (SiC), or 90 nm SiO_2/Si substrates. Following hBN exfoliation substrates were immersed in toluene overnight to remove tape residue, then blow-dried with N_2 before loading into a tube furnace to be annealed at 700 °C for 8 h under flowing H_2/Ar (5%, 0.15 slpm).

2.2. Ni particle etching

Ni was deposited on the substrates by thermal evaporation from high-purity Ni wire under high vacuum conditions (P $<$ 5.0 $\times$ 10^{-6} Torr). The deposition rate, monitored by a quartz crystal microbalance, was maintained at 0.02–0.04 nm s^{-1} to achieve nominal thicknesses of 0.2–0.4 nm. To produce a variable Ni particle density across the sample, some samples were placed a few millimetres below a shadow mask during deposition. Samples were then removed from vacuum and placed in the centre of a tube furnace under flowing H_2/Ar (5%, 0.15 slpm) and annealed 330 °C for 30 min, then ramped to the etching temperature (900 °C–1100 °C) and held for 60 min before cooling to room temperature, following the procedure reported in [27]. To remove the Ni particles, samples were chemically etched in HCl before rinsing in deionised water, acetone, isopropyl alcohol (IPA), and toluene.

Prior to graphene growth the samples were gently flame annealed or annealed in 5% H_2/Ar (0.15 slpm, 800 °C, 8 h) to remove solvent residue. The cleanliness of the samples was verified by AFM and x-ray photoemission spectroscopy (XPS) before graphene growth.

2.3. Graphene growth by molecular beam epitaxy

Graphene was grown in a customised dual chamber Veeco GENxplor high-temperature MBE system operating at a base pressure $\sim$10^{-10} mbar and growth temperatures of 1390 °C–1520 °C [21, 22]. Carbon flux was provided using a vertical electron beam evaporator (EBVV 63-T4, MBE Komponenten GmbH) with a high purity pyrolytic graphite target. The e-beam evaporator was operated at 5 kV accelerating voltage, and 250–350 mA emission current. The graphene coverage was controlled by varying the growth time in the range 2–8 min.

2.4. Material characterization

AFM images were acquired with an Asylum Research Cypher S instrument using Si cantilevers from NuNano (SCOUT 70 RAl) with a spring constant of 0.3 Nm (f_R = 70 kHz) in AC and contact modes. cAFM images were acquire using Pt/Cr coated Si cantilevers (SPARK 70Pt, NuNano) and bias voltages applied to the sample. All AFM images were processed and analysed using the Gwyddion software package [30].

X-ray photoemission spectra were acquired with a Kratos Axis Ultra instrument using a monochromated Al Kα source ($h\nu$ = 1486.7 eV). XPS data were analysed using the CasaXPS software package [31]. The energy scales were calibrated by a rigid shift of the spectra to align the C 1s core level peak for adventitious carbon at 285 eV.

Raman spectra were acquired with a Horiba LabRAM HR Raman microscope using a 532 nm excitation wavelength focused onto the sample through a 100$\times$ objective giving a spot size of 1 μm. The laser power was limited to $<$2 mW to prevent laser-induced heating or damage to the sample.

3. Results and discussion

Etched hBN layers were prepared by thermal evaporation of Ni onto hBN flakes exfoliated onto oxidised silicon and sapphire substrates, followed by annealing in a 5% H_2/Ar atmosphere. Figure 1(a) shows AC-AFM images of the h-BN surface after thermal evaporation of nominally 0.2 nm of Ni. This results in 63% surface coverage of few-nanometre sized Ni nano particles. During annealing at 900 °C the Ni particles become mobile on the surface and coalesce into larger Ni particles, which act as catalysts for the hydrogen etching of the hBN flakes. As a result, the Ni particles

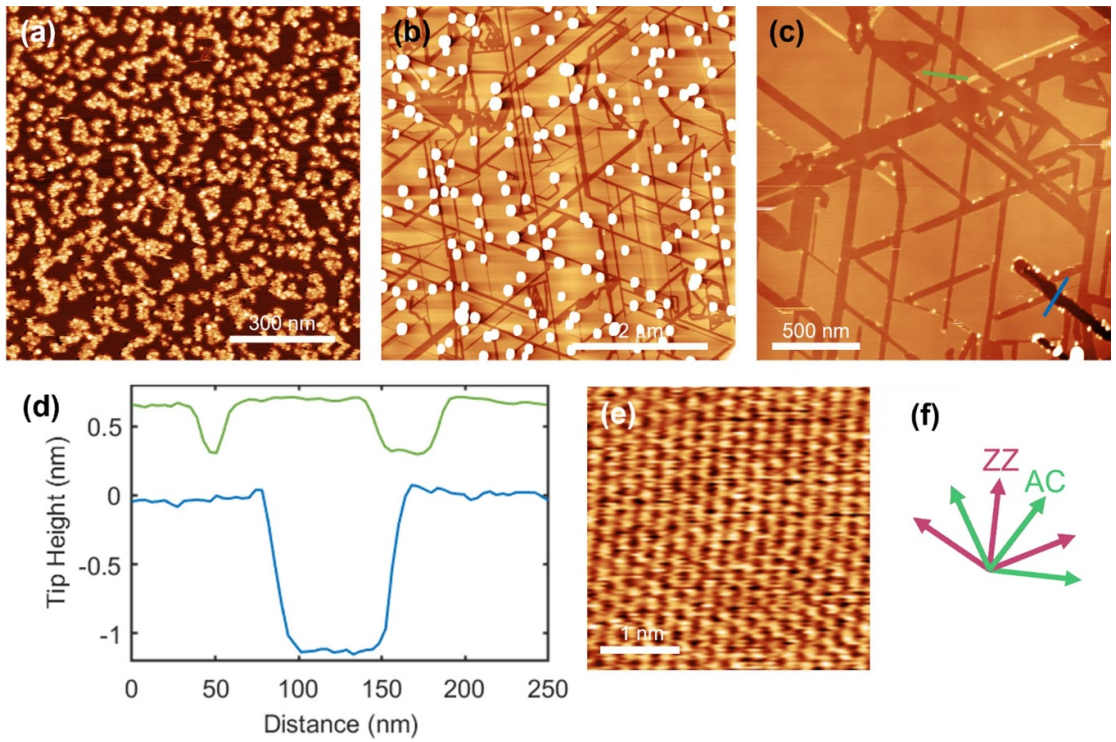

Figure 1. (a)–(c) AC-AFM images of the hBN surface and etch tracks (a) after thermal evaporation of a Ni layer with a nominal thickness of 0.2 nm; (b) after annealing Ni@hBN at 900 °C in 5% H_2/Ar for 1 h; (c) after Ni particle removal. (d) Tip height profiles taken along the green and blue lines in (c). (e) Contact mode AFM image showing lattice resolution of the etched hBN region in (c), (f) Zigzag (ZZ) and armchair (AC) lattice orientations extracted from the lattice image in (e).

create etch tracks in the hBN surface, as shown in the AC-AFM image in figure 1(b). A higher magnification image of the etch tracks after wet chemical etching to remove the Ni particles is shown in figure 1(c). From this image it is apparent that the etch tracks are remarkably straight and adopt a preferential orientation with respect the hBN crystal lattice as indicated by the 60° and 120° angles between the etch tracks. Lattice resolution imaging of the surface by contact mode AFM allows the lattice directions to be extracted, as shown in figures 1(e) and (f). From this it can be deduced that the Ni particles move preferentially along the zigzag (ZZ) lattice directions during the etching. The line profiles in figure 1(d) extracted from the AFM image in figure 1(c) show the presence of both monolayer (0.36 nm) and trilayer (1.1 nm) deep etch tracks. Broadly, the hBN samples contain predominantly monolayer deep etch tracks with very few etched bilayers or trilayers (figure S2, supplementary information). It is also noted that the trench edges are relatively free from contamination, and XPS measurements confirm that there is no detectable traces of Ni on the hBN surface after the wet chemical etch as shown in figure S1 (supplementary information).

We further analysed the temperature dependence on the etch track orientations and in figure 2. Figures 2(a)–(c) shows AFM images of the surface of etched samples with the same initial Ni coverage (0.63 ML). The corresponding distributions of the etch track orientations measured with respect to the horizontal axis of the images are shown in figures 2(d)–(f). At an etching temperature of 900 °C the etch tracks form preferentially along three symmetrically equivalent crystallographic orientations separated by 60°. As mentioned previously, these orientations correspond to the ZZ directions of the hBN lattice. Increasing the annealing temperature to 1000 °C results in a wider distribution of etch tracks with six preferred orientations separated by approximately 30°, although the distribution about each preferred orientation is notably broader. It can be inferred that in this case the tracks adopt both ZZ and armchair (AC) orientations. Increasing the etching temperature further to 1100 °C (figure 2(c)) results in Ni agglomeration to form larger particles and deeper etched pits in the surface. At the highest annealing temperature of 1100 °C several etch tracks exhibited sawtooth-like edges and triangular shaped pits were also observed on the surface, as indicated by the blue arrows in figure S3(a) (supplementary information). At this temperature, the Ni-catalysed etching occurs in conjunction with thermally activated hydrogen etching of the hBN step edges. This was confirmed by annealing hBN flakes in 5% H_2/Ar for prolonged periods without Ni particles, shown in figure S3(b), noting that without the Ni catalyst the etching requires much longer annealing times. Through changing the initial coverage of Ni particles and the annealing conditions we are able to achieve facile control of the etch track orientation and dimensions, as

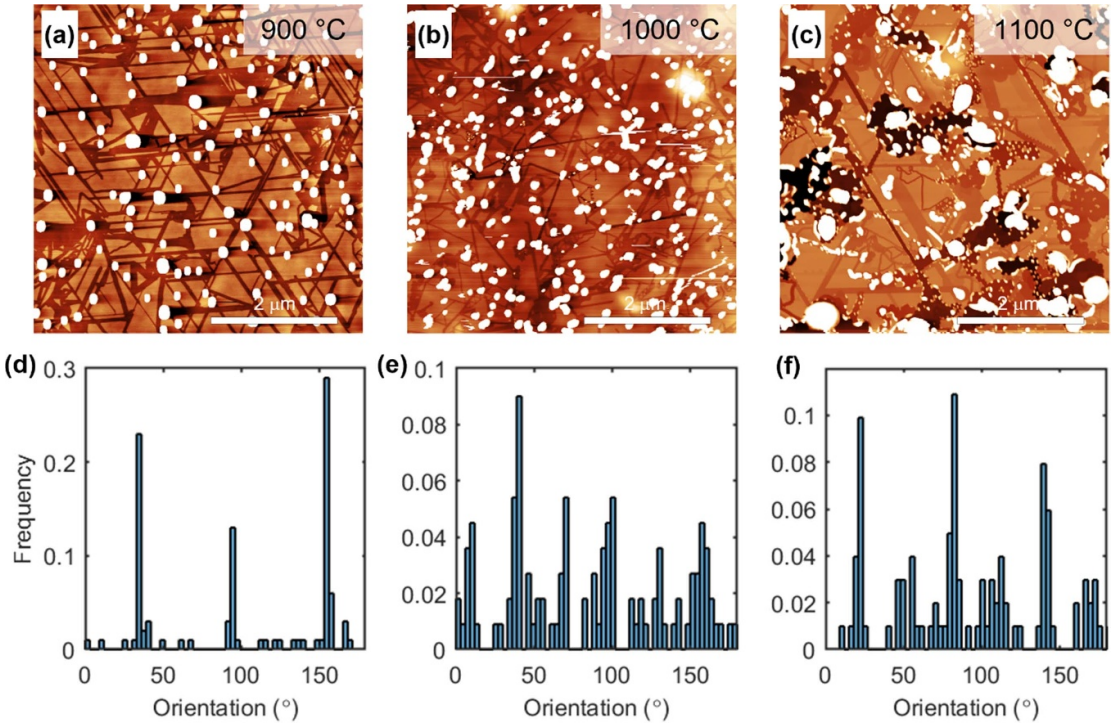

Figure 2. (a)–(c) AC-AFM images of Ni particle etched hBN flakes after annealing in 5% H_2/Ar for 60 min at (a) 900 °C, (b) 1000 °C, and (c) 1100 °C. (d)–(f) Histograms showing the distribution of etch track angles from images (a)–(c), in each, the orientation is measured with respect to the horizontal in the images. The absolute angles for the three histograms do not correlate with any particular crystallographic directions.

detailed further in figure S2 and associated discussion. In short, the etching temperature has a dominant effect on the Ni NP etching of hBN, but control of the Ni NP size through the initial coverage and ramp rate during annealing allows some tuneability of the width of the etched trenches.

The mechanism behind hBN etching using transition metal NP catalysts was recently studied theoretically by Ma *et al* [32]. The Ni particle plays a catalytic role in the dissociation of B–N bonds as well as the dissociation of the H_2 molecule, leading to the formation of gaseous NH_x and BH_x species, where the most favourable reaction is given by equation (1) [27]

$$2\mathrm{BN}\,(\mathrm{s}) + 6\mathrm{H_2}\,(\mathrm{g}) \xrightarrow{\mathrm{Ni}} \mathrm{B_2H_6}\,(\mathrm{g}) + 2\mathrm{NH_3}\,(\mathrm{g})\,. \qquad (1)$$

The cutting direction of the NPs is dictated by the interaction between the metal NP and exposed hBN edges. The most energetically favourable interactions occur between the Ni particle and either zigzag or armchair hBN edges rather than non-oriented edges. Generally, the etching direction will begin at step edges (as observed in figure S3(c)) and continue along a straight path until the particle reaches a hBN step edge or defect, at which point the Ni particle's path will change to maintain the interaction with hBN on both sides of the Ni particle and continue along a new path. This gives rise to the types etching patterns seen in figure S3(d) where a particle 'bounces' between existing etch tracks to produce nano-sized hBN triangles.

Following removal of the Ni NPs by wet chemical etching, graphene was grown on the etched hBN flakes by HT-MBE. AC- AFM images in figures 3(a)–(c) show GNRs formed around the edges of hBN etch tracks after graphene growth for 2 min at a substrate temperature of ∼1390 °C. The topographic images reveal a height difference of around ∼0.1 nm between the hBN and graphene, as well as good phase contrast that allows identification of the graphene strip. This is shown in the line profiles in figure 3(d) which are taken along the identical paths indicated in figures 3(b) and (c), and the graphene regions are shaded in yellow. Consistent with previous results, the step flow growth of graphene from hBN edges results in GNRs with a uniform width distribution [21, 22]. These growth conditions produce nanoribbons with a width of 11.1 ± 1.8 nm, with the distribution of the nanoribbon widths as measured by AFM shown in figure 3(e). Where the width of the hBN trenches is sufficiently narrow (or by extending the growth time, as discussed later), the two opposing growth fronts can merge seamlessly to produce GNRs embedded in the top layer of the hBN flake. An example of this is shown

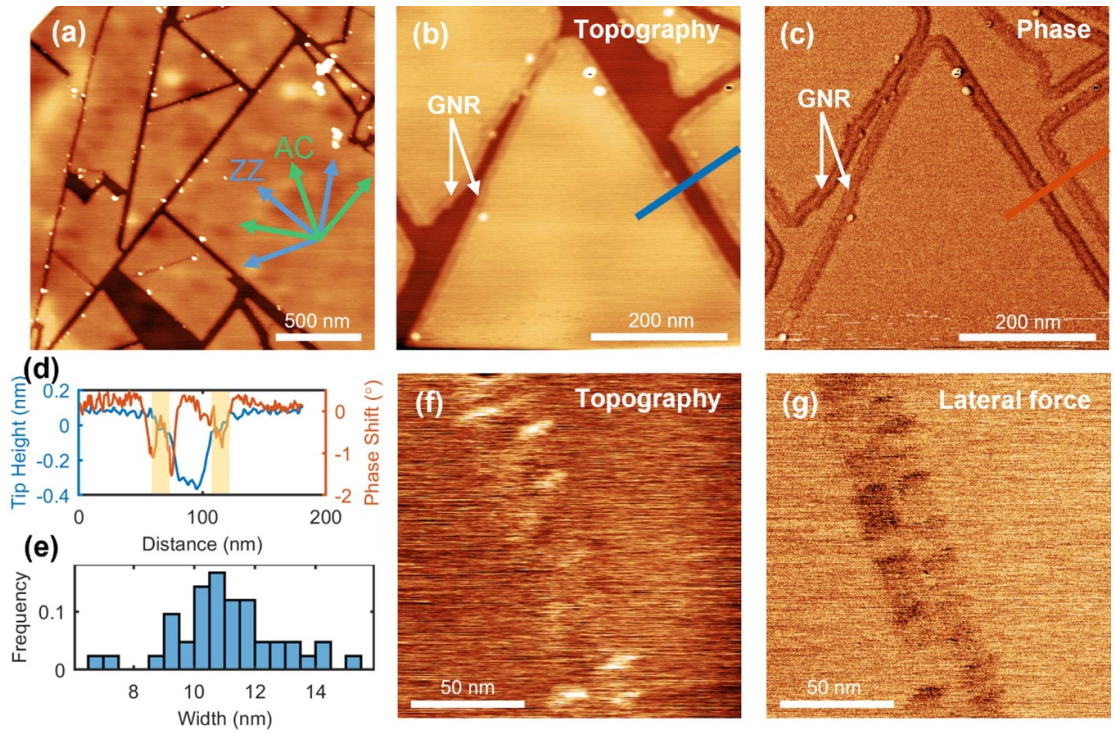

Figure 3. AFM analysis of the surface after 2 min HT-MBE graphene growth. (a) AC-AFM topography image of the edge-templated GNRs grown on etched hBN. The inset arrows show the zigzag and armchair directions of the hBN lattice determined by lattice resolution imaging. (b) Higher magnification AC-AFM image showing graphene growth from hBN step edges, with the GNRs indicated by the white arrows. (c) Phase contrast of the same region in (b). (d) Line profiles taken along the same line in topography and phase images as indicated in (b) and (c). The yellow shaded regions show indicate the graphene areas. (e) Histogram showing the distribution of the GNR widths. (f) Topography, and (g) lateral force signal measured in contact mode over a fully merged GNR.

in the high-resolution contact mode images are shown in figures 3(f) and (g). The topography image in figure 3(f) shows virtually no height difference between the GNR and the hBN surface, but contrast in the lateral force signal shown in figure 3(g) enables clear identification of a 33 nm wide ZZ-GNR. A moiré pattern with a period of ∼15 nm along the length of the GNR (figures S4(a) and (b), supplementary information) suggests that the graphene is strained by ∼0.14% along this direction [33]. Across all samples we observe moiré periods of up to 25.8 nm in graphene corresponding to a strain of ∼0.84% (figures S4(c) and (d)). We note that graphene growth is only observed on monolayer step edges, and multilayer step edges tend to nucleate carbon clusters, as shown in figures S4(e) and (f), which we have similarly observed for the growth of hBN on highly oriented pyrolytic graphite [22].

For samples grown at higher substrate temperatures we observe differences in GNR growth depending on the termination of the hBN edge from which it is nucleated. Figure 4(b) shows a large area image of partially filled GNRs grown at a substrate temperature of 1480 °C. The region contains etch tracks of both ZZ and AC orientation, where the orientations indicated by the arrows are determined from lattice resolution imaging of the hBN (figure 4(e)). Lattice images of the neighbouring GNR (figure 4(f)) confirm that the GNR is laterally epitaxial to the hBN edge, which is consistent with our previous observations for lateral heterojunctions formed by sequential growth of hBN and graphene layers [21, 22].

Figures 4(c) and (d) show in higher detail the regions marked by the blue and green squares, respectively (enlarged copies can be seen in figures S5(b) and (c), supplementary information). In these images the GNRs can be identified as slightly raised borders on hBN step edges. For GNRs grown from hBN AC edges, as shown in figure 4(c), there are no obvious differences between the growth from opposing edges. The graphene grows to produce nanoribbons which are approximately uniform in width, and the exposed graphene edge generally reflects the morphology of the nucleating hBN edge. For graphene growth from opposing ZZ edges of the same hBN etch track, there are clear differences in the GNR with and edge morphology. This is exemplified by the growth around a triangular hBN island shown in figure 4(d). The inner hBN edges of the triangle all have a common edge termination and have produced wider GNRs with jagged edges. We note that no discernible difference in edge roughness was observed prior to graphene growth, or on GNRs grown at lower temperatures (∼1390 °C, figures 3(a)–(c)) suggesting that the edge roughness may be related to the stability of one of the hBN ZZ edges at high temperature.

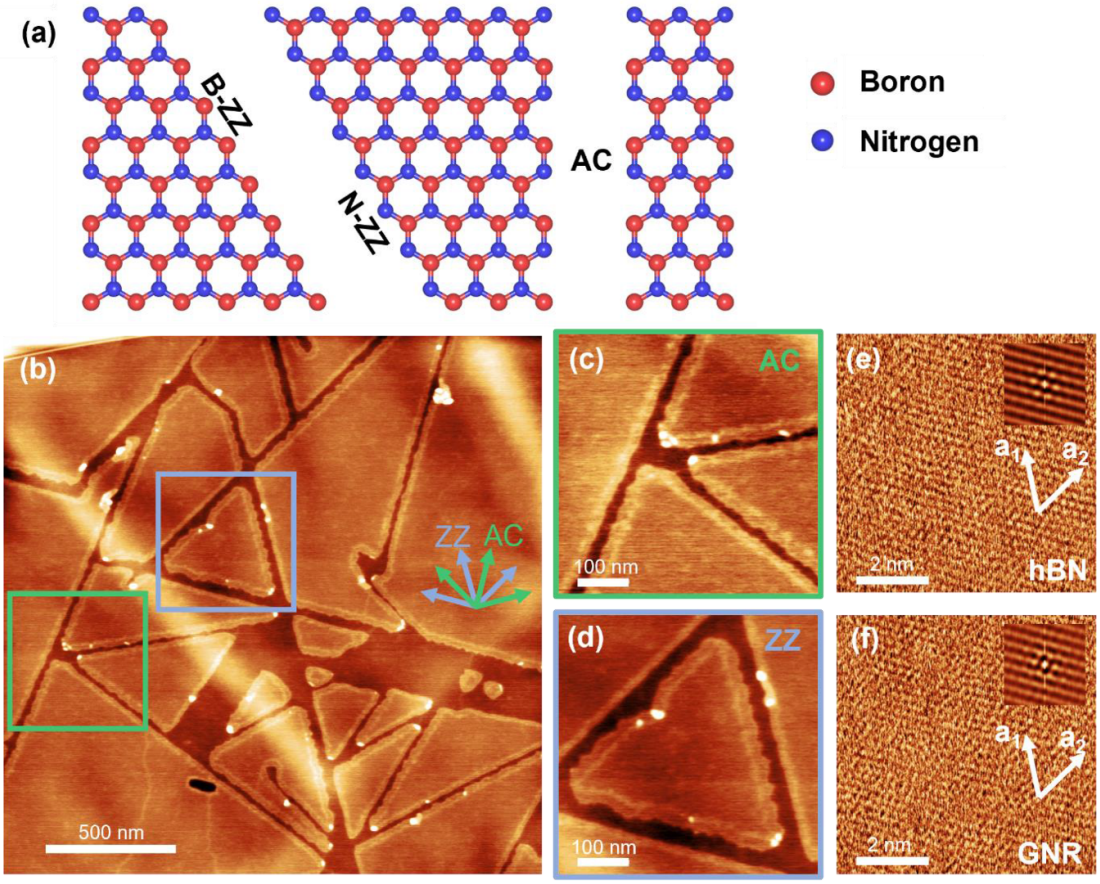

Figure 4. (a) Atomic model of a hBN monolayer with cuts along the zigzag direction (left) with opposing boron (B-ZZ) and nitrogen (N-ZZ) terminations, and armchair direction (right); (b) AC-AFM image of GNRs grown at a substrate temperature of 1480 °C. Inset arrows shows the hBN zigzag and armchair directions determined from lattice resolution imaging; (c) magnified view of the green box in (b) showing a set of armchair oriented GNRs; (d) magnified view of the blue box in (b) showing a set of zigzag oriented GNRs; (e), (f) lattice resolution images of hBN and graphene, respectively. The insets show 2D autocorrelation function (ACF) images used to identify the lattice directions shown by the white arrows.

In contrast, on the outer hBN edges, which possess the opposite edge termination, the growth results in relatively narrow GNRs with smooth edges. We note that this has been observed across multiple samples, and at different relative scan angles, thus tip effects on the measured width of the GNRs can be ruled out. Across all oriented etch tracks shown in figure 4(a), the difference in width of opposing GNRs is measured to be 14.9 ± 8.7 nm for ZZ oriented nanoribbons, and 2.9 ± 1.2 nm for AC oriented ribbons (see figure S6 and table S1, supplementary information).

When an etch track in a hBN monolayer is formed parallel to the zigzag direction, the two edges have a different atomic termination. As shown in figure 4(a) one B-terminated edge (B-ZZ) and one N-terminated edge (N-ZZ) are formed on either side of the track. The different edge terminations are not equivalent, and our observation that different GNR widths are formed on opposing edges implies that the energetics and related mechanisms of graphene growth are different on the two edges. Although we are able to acquire AFM images with atomic-scale resolution in our experimental configuration it is not possible to distinguish between B and N atoms in our images. Nevertheless, it is useful to consider the two main factors that are likely to contribute to faster graphene growth along one of the ZZ edges compared to the other: the energy of C–B and C–N interfaces, and nanoscale roughness of the edges. C–B-ZZ interfaces have previously been determined to be the most energetically favourable interface between graphene and hBN, which may lead to preferential graphene nucleation along the B-ZZ edge [18, 19]. However, if the differences were governed by interfacial energetics alone, it might be expected that the differences would be observed across a range of temperatures; in fact we observe smooth edges on GNRs grown on both ZZ terminations at ∼1390 °C (figures 3(a)–(c)), and a uniform width distribution (figure 3(e)), whereas at higher growth temperatures (∼1480 °C) we observe roughening of the edge of the wider GNR which

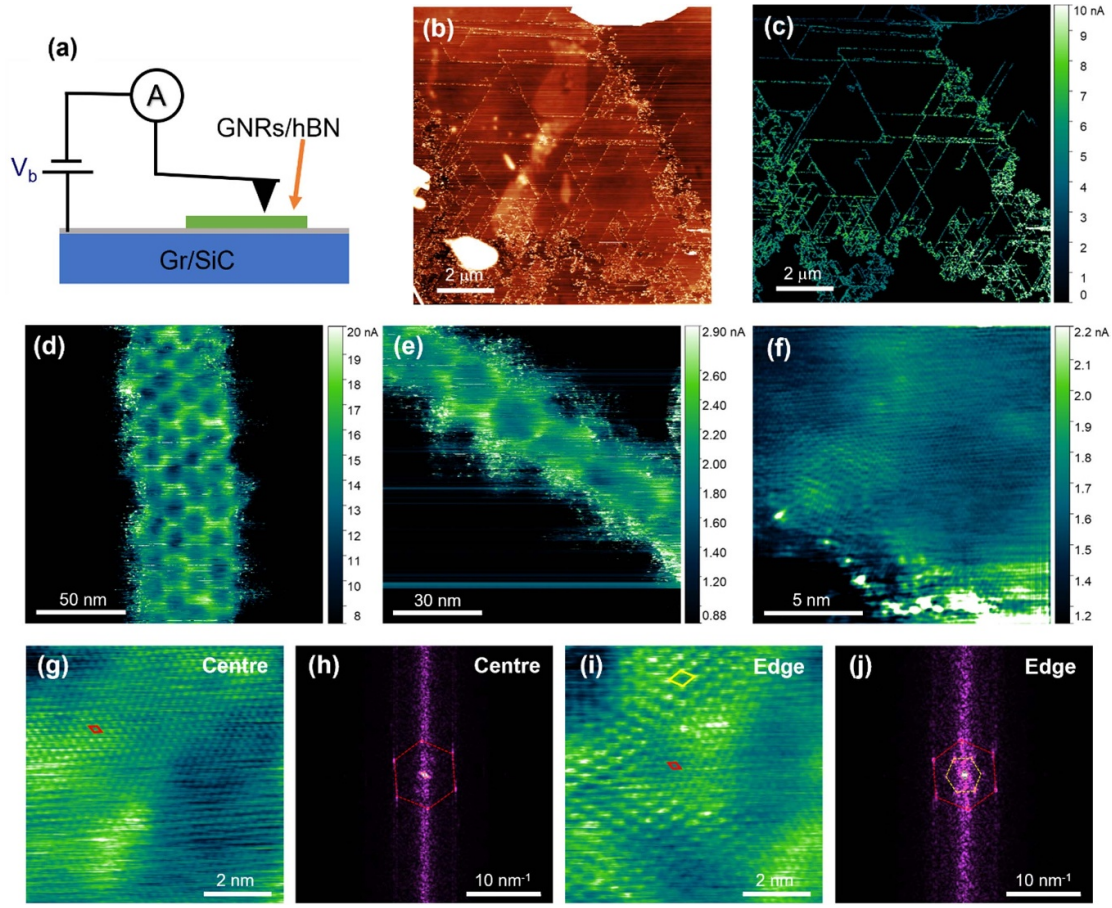

Figure 5. (a) Schematic diagram of the cAFM measurement; (b) topography and (c) current map of the hBN surface after graphene growth for 4 min at a substrate temperature of 1440 °C. (d)–(f) High-resolution cAFM current maps of GNRs grown for 4 min at a substrate temperature of 1480 °C. (d) and (e) show moiré modulation of the current, and (f) reveals lattice features of the nanoribbon. (g) and (i) show lattice resolution cAFM images taken from the centre (g) and edge (i) of the GNR. (h) and (j) show the 2D fast Fourier transform (FFT) patterns from images (g) and (i), respectively. Fourier filtering has been applied to enhance the lattice features in (g) and (i), but the corresponding FFTs are from the raw data. Surface bias voltages, V_b, are (c), (d) 50 mV, (e) 20 mV, (f) 10 mV, and (g), (i) 30 mV.

occurs on a common ZZ termination. Increasing the growth temperature further to above 1520 °C results in apparent breakdown of the hBN edges and widening of the etch tracks (see figure S7, supplementary information). This temperature dependence is likely due to the relative stability of the etched hBN edges which may lead to nanoscale roughness of the edges, enabling faster graphene growth. Noting that the N-ZZ edge is predicted to have higher stability than the B-ZZ edge [4, 34], both factors lead us to tentatively assign faster GNR growth from the B-ZZ hBN edge.

The GNRs were further characterised by Raman spectroscopy as shown in figure S8 (supplementary information). The spectrum shows the Raman signature of graphene with peaks at 1345 cm^{-1}, 1586 cm^{-1} and 2688 cm^{-1} corresponding to the D, G and 2D vibrational modes. In addition, a high frequency shoulder at 1623 cm^{-1} is the defect-related D′ peak, and the D + D′ overtone is visible at 2973 cm^{-1}. In addition to the graphene-related peaks, a sharp peak at 1365 cm^{-1} is attributed to the E_{2g} LO phonon mode of hBN. The graphene peak positions align well with those observed for minimally strained monolayer graphene grown on hBN by HT-MBE [33, 35], and for exfoliated monolayers [36], although the features are slightly broadened (see table S2, supplementary information) which may be due to nanoscale strain variations [37]. The relatively high intensity of the D band relative to G is to be expected considering the high edge density of the nanoribbons.

Figure 5 shows cAFM measurements of the GNR network formed by extending the growth time to completely fill the hBN trenches. In order to form a conducting pathway, hBN flakes were exfoliated onto a graphitised SiC surface. Provided the GNR network extends to the edge of the hBN flake, a conductive pathway to an external electrode can be formed via the conducting, graphitised surface (see figure 5(a)), and the GNRs can be probed by cAFM. The contact mode topography and a corresponding current map shown in figures 5(b) and (c), respectively, clearly shows the conductive GNR network. Figure 5(c) shows the cAFM signal from a 50 nm wide GNR

where modulation of the current according to the moiré period is observed, consistent with previous cAFM measurements of graphene monolayers grown on hBN by HT-MBE [35]. The moiré pattern exhibits 17.8 nm periodicity along the length of the GNR, and 14.1 nm across the transverse direction, suggesting ∼0.40% uniaxial strain along the length of the nanoribbon. The variation in conductivity is due to the commensurate–incommensurate transition of graphene on hBN where lattice mismatch induced strain is localised to Frenkel–Kontorova (F−K) domain walls [35, 38]. Regions where the graphene is commensurate to the hBN (moiré valleys) possess a small band gap (∼50 meV) and thus a lower density of states (and conductivity) compared to the incommensurate graphene (moiré peaks) [35]. This effect is observed even at the limit where the width of the nanoribbon is approximately equal to one moiré period, in which case a 1D moiré superlattice with 17.4 nm period is formed as shown in figure 5(e). Similar 1D moiré patterns have been observed for GNRs grown on hBN, but were not observed to exhibit any strain [39]. We propose that the strain induced by high temperature growth can be sustained through bonding at the graphene/hBN interface. Interestingly, we do not observe any grain boundaries or regular defects running parallel to the graphene/hBN interfaces, regardless of the width or orientation of the nanoribbons, indicating atomically precise merging of the two growth fronts from opposite hBN step edges.

High-resolution imaging of the GNRs reveals the lattice structures shown in figure 5(f). An ordered lattice is visible in the centre of the GNR (figure 5(g)) with a 0.25 ± 0.01 nm lattice constant, as expected for graphene, and the corresponding fast Fourier transform (FFT) in figure 5(h) shows only (1 × 1) graphene spots. Close to the graphene/hBN interface, in figure 5(i), a $(\sqrt{3}\times\sqrt{3})$R30° superstructure (unit cell marked in yellow) is visible in addition to the graphene lattice (red unit cell). These structures are also visible in the FFT (figure 5(j)) marked by the yellow and red hexagons, respectively. The $(\sqrt{3}\times\sqrt{3})$R30° superstructure in graphene is due to a quasiparticle interference standing wave caused by intervalley scattering between K and K′ Dirac points close to the Fermi level [40, 41]. Such scattering requires local, short-range breaking of the sublattice symmetry by atomic scale defects [40] and edges [41, 42]. Intervalley scattering has been commonly observed at armchair and disordered edges, whereas zigzag edges show only intravalley scattering [41]. Previous scanning tunnelling microscopy studies of atomically precise graphene/hBN zigzag interfaces do not report observations of intervalley scattering, suggesting that there is disorder at the graphene/hBN interface in our system [16, 19].

It is somewhat unsurprising to observe carrier scattering at the interface considering the lattice mismatch between graphene and hBN. Even in the case of a perfectly formed interface, the lattice mismatch necessitates the presence of regular edge dislocations to relieve strain at the interface [43, 44]. Given the understood commensurate–incommensurate transition of graphene on hBN, it is logical that the defect would occur at the termination of a F−K domain wall, similar to our previous observations in strained graphene [35]. Although we cannot precisely locate or identify atomic scale defects at the graphene/hBN interface, on samples with higher graphene coverage we have observed the formation of small atomic clusters at regular intervals along the interface. An example of this is shown in figure S9 (supplementary information) where the spacing of these clusters is close the moiré period in the GNR. These features suggest that defects at the interface may act as nucleation points for further graphene growth. Once growth is initiated, the second graphene layer can as a bilayer over the GNR or a monolayer on hBN, which is also visible in figure S9. Considering our previous work on strain engineering and lattice matching of graphene grown on hBN by HT-MBE [33, 35], we have attempted to improve the quality of the interface by increasing growth temperatures to those where lattice-matching was observed. However, at temperatures exceeding 1520 °C we observe break down and desorption of the hBN at step edges, which leads to widening of the trenches and no clear graphene growth (figure S7).

4. Conclusion

We have demonstrated the growth of highly oriented GNR networks embedded in hBN using HT-MBE to grow graphene on a Ni NP etched hBN surface. The Ni NP etching process energetically favours the formation of zigzag oriented, monolayer deep etch tracks at reduced etching temperatures, and the inclusion of armchair oriented etch tracks at high temperatures. Subsequent graphene growth by HT-MBE shows a substrate temperature dependence on the uniformity of the growth rate from zigzag oriented hBN edges, but ultimately seamless merging of the growth fronts to form hBN passivated GNRs. High-resolution cAFM has been used to probe electronic transport in GNRs at the nanoscale and provides direct evidence of quasiparticle interference due to intervalley scattering at the graphene/hBN interface. This highlights the need for further advances in the controlled formation of long-range, atomically precise interfaces between hBN and graphene to fully utilise them in atomically thin electronic devices and circuitry.

Data availability statement

The data that support the findings of this study are openly available at the following URL/DOI: http://doi.org/10.17639/nott.7273.

Acknowledgments

The authors thank the Nanoscale and Microscale Research Centre (nmRC) for providing access to instrumentation, and Dr Emily Smith and Dr Craig Stoppiello for technical assistance. We would like to acknowledge Prof L Eaves and Prof C T Foxon for their continuous help and advice. This work was supported by the Engineering and Physical Sciences Research Council UK (Grant Numbers EP/K040243/1, EP/P019080/1 and EP/V05323X/1).

ORCID iDs

Jonathan Bradford https://orcid.org/0000-0003-2356-5816
Tyler S S James https://orcid.org/0000-0002-9681-1558
Andrei N Khlobystov https://orcid.org/0000-0001-7738-4098
Christopher J Mellor https://orcid.org/0000-0001-5987-7876
Kenji Watanabe https://orcid.org/0000-0003-3701-8119
Sergei V Novikov https://orcid.org/0000-0002-3725-2565
Peter H Beton https://orcid.org/0000-0002-2120-8033

References

[1] Levendorf M P, Kim C J, Brown L, Huang P Y, Havener R W, Muller D A and Park J 2012 Graphene and boron nitride lateral heterostructures for atomically thin circuitry *Nature* **488** 627–32
[2] Liu Z *et al* 2013 In-plane heterostructures of graphene and hexagonal boron nitride with controlled domain sizes *Nat. Nanotechnol.* **8** 119–24
[3] Li Q, Liu M, Zhang Y and Liu Z 2016 Hexagonal boron nitride-graphene heterostructures: synthesis and interfacial properties *Small* **12** 32–50
[4] Liu Y, Bhowmick S and Yakobson B I 2011 BN white graphene with “Colorful” edges: the energies and morphology *Nano Lett.* **11** 3113–6
[5] Li K and Zhang X H 2018 Asymmetrical edges induced strong current-polarization in embedded graphene nanoribbons *Phys. Lett.* A **382** 1167–70
[6] Song L, Zhang Y, Ye R, Liu L, Wei C, Zhao H and Zheng X 2022 h-BN as a perfect spin splitter in ferromagnetic zigzag graphene nanoribbons *2D Mater.* **10** 015017
[7] Li J and Shenoy V B 2011 Graphene quantum dots embedded in hexagonal boron nitride sheets *Appl. Phys. Lett.* **98** 13105
[8] Fan X, Shen Z, Liu A Q and Kuo J-L 2012 Band gap opening of graphene by doping small boron nitride domains *Nanoscale* **4** 2157–65
[9] Wang J, Zhao R, Liu Z and Liu Z 2013 Widely tunable carrier mobility of boron nitride-embedded graphene *Small* **9** 1373–8
[10] Zhang D, Zhang D-B, Yang F, Lin H-Q, Xu H and Chang K 2015 Interface engineering of electronic properties of graphene/boron nitride lateral heterostructures *2D Mater.* **2** 41001
[11] Bhowmick S, Singh A K and Yakobson B I 2011 Quantum dots and nanoroads of graphene embedded in hexagonal boron nitride *J. Phys. Chem.* C **115** 9889–93
[12] Zhao R, Wang J, Yang M, Liu Z and Liu Z 2012 BN-embedded graphene with a ubiquitous gap opening *J. Phys. Chem.* C **116** 21098–103
[13] Ding Y, Wang Y and Ni J 2009 Electronic properties of graphene nanoribbons embedded in boron nitride sheets *Appl. Phys. Lett.* **95** 123105
[14] Wang M, Li X, Li Y, Zuo X, Li D, Cui B and Liu D-S 2018 Impact of interface types on spin transport in heterostructures of graphene/hexagonal boron-nitride nanoribbons *Org. Electron.* **58** 63–68
[15] Ci L *et al* 2010 Atomic layers of hybridized boron nitride and graphene domains *Nat. Mater.* **9** 430–5
[16] Liu L, Park J, Siegel D A, McCarty K F, Clark K W, Deng W, Basile L, Idrobo J C, Li A-P and Gu G 2014 Heteroepitaxial growth of two-dimensional hexagonal boron nitride templated by graphene edges *Science* **343** 163–7
[17] Sutter P, Huang Y and Sutter E 2014 Nanoscale integration of two-dimensional materials by lateral heteroepitaxy *Nano Lett.* **14** 4846–51
[18] Drost R, Uppstu A, Schulz F, Hämäläinen S K, Ervasti M, Harju A and Liljeroth P 2014 Electronic states at the graphene–hexagonal boron nitride zigzag interface *Nano Lett.* **14** 5128–32
[19] Drost R, Kezilebieke S, M. Ervasti M, Hämäläinen S K, Schulz F, Harju A and Liljeroth P 2015 Synthesis of extended atomically perfect zigzag graphene—boron nitride interfaces *Sci. Rep.* **5** 16741
[20] Camilli L, Jørgensen J H, Tersoff J, Stoot A C, Balog R, Cassidy A, Sadowski J T, Bøggild P and Hornekær L 2017 Self-assembly of ordered graphene nanodot arrays *Nat. Commun.* **8** 47
[21] Thomas J *et al* 2020 Step-flow growth of graphene-boron nitride lateral heterostructures by molecular beam epitaxy *2D Mater.* **7** 035014
[22] Wrigley J *et al* 2021 Epitaxy of boron nitride monolayers for graphene-based lateral heterostructures *2D Mater.* **8** 034001
[23] Gong Y *et al* 2014 Direct chemical conversion of graphene to boron- and nitrogen- and carbon-containing atomic layers *Nat. Commun.* **5** 3193
[24] Bradford J, Shafiei M, MacLeod J and Motta N 2019 Transfer-free synthesis of lateral graphene–hexagonal boron nitride heterostructures from chemically converted epitaxial graphene *Adv. Mater. Interfaces* **6** 1900419
[25] Kim G, Lim H, Ma K Y, Jang A-R, Ryu G H, Jung M, Shin H-J, Lee Z and Shin H S 2015 Catalytic conversion of hexagonal boron nitride to graphene for in-plane heterostructures *Nano Lett.* **15** 4769–75
[26] Chen L *et al* 2017 Oriented graphene nanoribbons embedded in hexagonal boron nitride trenches *Nat. Commun.* **8** 14703
[27] Ansary A, Nasseri M, Boland M J and Strachan D R 2018 Parallel boron nitride nanoribbons and etch tracks formed through catalytic etching *Nano Res.* **11** 4874–82
[28] Wang H H S *et al* 2021 Towards chirality control of graphene nanoribbons embedded in hexagonal boron nitride *Nat. Mater.* **20** 202–7
[29] Chen C *et al* 2022 Directional etching for high aspect ratio nano-trenches on hexagonal boron nitride by catalytic metal particles *2D Mater.* **9** 025015
[30] Nečas D and Klapetek P 2012 Gwyddion: an open-source software for SPM data analysis *Cent. Eur. J. Phys.* **10** 181–8
[31] Fairley N*et al* 2021 Systematic and collaborative approach to problem solving using X-ray photoelectron spectroscopy *Appl. Surf. Sci.* **5** 100112

[32] Ma L and Zeng X C 2017 Catalytic directional cutting of hexagonal boron nitride: the roles of interface and etching agents *Nano Lett.* **17** 3208–14
[33] Summerfield A *et al* 2016 Strain-engineered graphene grown on hexagonal boron nitride by molecular beam epitaxy *Sci. Rep.* **6** 22440
[34] Fu X and Zhang R 2017 Energetics of hexagonal boron nitride nanostructures: edge dependence and truncation effects *Nanoscale* **9** 6734–40
[35] Davies A *et al* 2018 Lattice-matched epitaxial graphene grown on boron nitride *Nano Lett.* **18** 498–504
[36] Ferrari A C *et al* 2006 Raman spectrum of graphene and graphene layers *Phys. Rev. Lett.* **97** 187401
[37] Neumann C *et al* 2015 Raman spectroscopy as probe of nanometre-scale strain variations in graphene *Nat. Commun.* **6** 1–7
[38] Woods C R *et al* 2014 Commensurate–incommensurate transition in graphene on hexagonal boron nitride *Nat. Phys.* **10** 451
[39] Lyu B *et al* 2022 Catalytic growth of ultralong graphene nanoribbons on insulating substrates *Adv. Mater.* **34** 2200956
[40] Rutter G M, Crain J N, Guisinger N P, Li T, First P N and Stroscio J A 2007 Scattering and interference in epitaxial graphene *Science* **317** 219–22
[41] Xu P *et al* 2012 Quasiparticle scattering off phase boundaries in epitaxial graphene *Nanotechnology* **23** 055706
[42] Yang H, Mayne A J, Boucherit M, Comtet G, Dujardin G and Kuk Y 2010 Quantum interference channeling at graphene edges *Nano Lett.* **10** 943–7
[43] Lu J, Gomes L C, Nunes R W, Castro Neto A H and Loh K P 2014 Lattice relaxation at the interface of two-dimensional crystals: graphene and hexagonal boron-nitride *Nano Lett.* **14** 5133–9
[44] Nandwana D and Ertekin E 2015 Ripples, strain, and misfit dislocations: structure of graphene–boron nitride superlattice interfaces *Nano Lett.* **15** 1468–75